Linear viscoelasticity of anisotropic carbon fibers reinforced thermoplastics: from micromechanics to dynamic torsion experiments

Thomas Merlette, Julie Diani

Graphical Abstract

Linear viscoelasticity of anisotropic carbon fibers reinforced thermoplastics: from micromechanics to dynamic torsion experiments

Thomas C. Merlette, Julie Diani

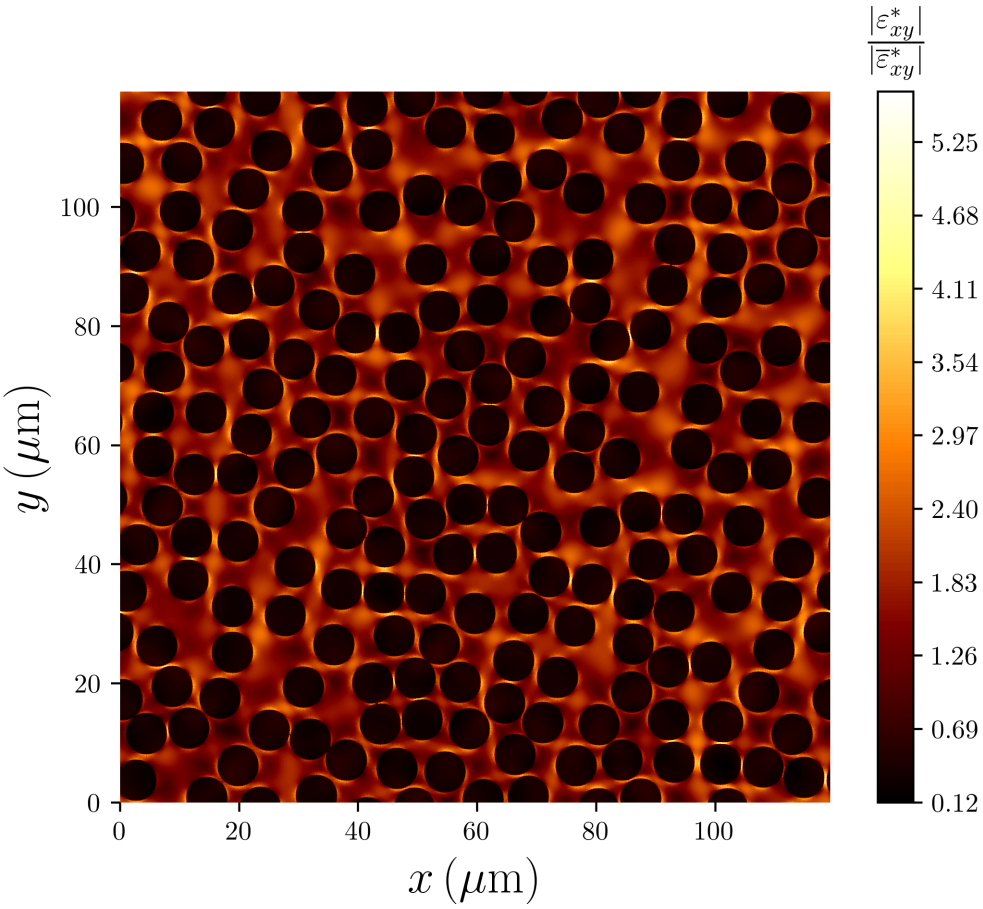

Highlights

Linear viscoelasticity of anisotropic carbon fibers reinforced thermoplastics: from micromechanics to dynamic torsion experiments

Thomas C. Merlette, Julie Diani

- FFT-based homogenization of viscoelastic properties of carbon fiber reinforced polymers in the frequency domain
- Transversely isotropic linear viscoelasticity characterization and modeling
- Impact of spatial arrangement of fibers on effective viscoelastic properties in glassy and rubbery states
- Comparison between DMA experiments and predictions in glassy and rubbery states
- Dynamic Mechanical Analysis experiments and Finite element simulations in the frequency domain

Linear viscoelasticity of anisotropic carbon fibers reinforced thermoplastics: from micromechanics to dynamic torsion experiments

Thomas C. Merlette[a,*], Julie Diani[a]

[a] *Laboratoire de Mécanique des Solides, CNRS UMR 7649, Ecole Polytechnique, Institut Polytechnique de Paris, Route de Saclay, Palaiseau, 91128, France*

Abstract

The link between experimental characterization and the constitutive behavior of an anisotropic linear viscoelastic unidirectional carbon fiber-reinforced thermoplastic composite is explored using micromechanics modeling. Dynamic torsion tests were conducted at 1 Hz over a wide temperature range, from the glassy to the rubbery states of the polymeric matrix, on both the pure matrix and the composite, for various cutting angles relative to the fibers. A two-step modeling procedure in the frequency domain is presented to predict and validate the effective behavior of the composite. The first step involves FFT-based homogenization, which maps the microstructure and constituent behaviors to effective transversely isotropic viscoelastic properties. The second step consists of finite element simulations using the effective behavior calculated from homogenization as input to replicate the experiments. A comparison between experimental results and model predictions across the entire temperature range is performed. The modeling predictions show good accuracy at low temperatures, where the matrix is in the glassy state. At high temperatures, where the matrix is in the rubbery state, the predicted behavior becomes too soft. As the phase contrast increases and the ratio of matrix bulk modulus to shear modulus rises significantly, the impact of fiber arrangement on the effective properties becomes more pronounced.

Keywords: FFT-based homogenization, Carbon fibers, Polymers, Anisotropy, Viscoelasticity, Dynamic Mechanical Analysis

*Corresponding author

Email address: thomas.merlette@polytechnique.edu (Thomas C. Merlette)

1. Introduction

Unidirectional (UD) carbon fiber-reinforced polymers are advanced materials known for their exceptional strength-to-weight ratio and stiffness, making them ideal for applications in aerospace, transportation, storage, and sports equipment. These materials exhibit viscoelastic behavior due to the polymer matrix, which can be advantageous for energy dissipation, such as in vibration reduction, but problematic when it leads to undesired creep for instance. Thermoplastic matrices are gaining popularity over thermosets due to their recyclability, though their potential for flow in certain industrial applications necessitates accurate predictions of their viscoelastic behavior. In typical applications, the fiber volume fraction ranges between 50% and 60%. This study focuses on a thermoplastic matrix filled with 53% long aligned carbon fibers, used in hydrogen tanks. Given that these tanks experience constant loads over extended periods, understanding the viscoelastic behavior across a wide temperature range is crucial for predicting long-term creep.

In the mechanical characterization of the viscoelastic properties of such composites, several measurement techniques and mechanical tests operate either in the time or frequency domain, such as creep, stress relaxation, dynamic mechanical analysis (DMA), or wave attenuation (Lakes, 2004). However, experimental characterization is not standardized and is often dependent on the specific setup (Treviso et al., 2015). DMA is a common and widely used technique for isotropic materials because it provides measurements over a wide range of temperatures and frequencies. Its use has been extended to UD composites, which are typically transversely isotropic. For these materials, dynamic torsion tests (Huayamares et al., 2020) or 3-point bending tests (Pathan et al., 2017a; Melo and Radford, 2005; Huayamares et al., 2020) are common methods. The 3-point bending test is usually preferred due to the absence of clamping effects, though it requires large sample dimensions (Swaminathan and Shivakumar, 2009). It may also be limited in temperature range, as the unclamped sample might not follow the imposed oscillations at high temperatures, depending on the angle between the sample and the fibers (Ropers et al., 2017). DMA characterization studies often assume that a direct measurement of material viscoelastic parameters is possible, though this is rarely verified or discussed.

In terms of modeling, micromechanical models allow for scale-transition,

enabling the prediction of the effective properties of the composite based on the behavior and spatial arrangement of its phases. The linear elastic properties of UD composites have been extensively studied over the past few decades. Mean-field models were proposed (Hashin and Rosen, 1964; Christensen and Lo, 1979; Mori and Tanaka, 1973; Huang, 2000; Chamis, 1989; Halpin and Tsai, 1969), as detailed in the review by (Vignoli et al., 2019). Full-field methods, primarily finite element homogenization approaches (Sun and Vaidya (1996); Xia et al. (2003); Huang et al. (2008), among others), have been employed to evaluate both the efficiency of mean-field models and the influence of microstructure and phase behaviors. Micromechanical modeling of effective elastic properties has mainly focused on temperatures below the glass transition temperature, with attention to the impact of fiber volume fraction and spatial distribution (Oh et al. (2006); Huang et al. (2008); Vignoli et al. (2019); Younes et al. (2012), among others). Beicha et al. (2016) investigated the effect of phase contrast on elastic properties, assuming isotropic phases and a constant matrix Poisson's ratio. Their study showed a significant influence of fiber spatial arrangement on effective elastic properties, particularly for high fiber volume fractions and high phase contrast.

In the linear regime of steady-state harmonic oscillations, elastic mean-field models can be extended to linear viscoelastic ones in the frequency domain using the elastic-viscoelastic correspondence principle (Hashin, 1970). Micromechanical models can also access viscoelastic properties in both the time and frequency domains. Recently, Gusev and Kern (2018) applied finite element homogenization to demonstrate that the mean-field 3-phase cylinder model (Hashin and Rosen, 1964; Christensen and Lo, 1979) accurately reproduces the effective linear viscoelastic properties of an epoxy matrix reinforced by either long transversely isotropic carbon fibers or long isotropic glass fibers. Their numerical study focused on low temperatures (with the matrix in the glassy state) and varying fiber volume fractions. Tsai and Chi (2008) highlighted the impact of different periodic fiber arrangements on loss factors in the glassy state. However, few studies have investigated the effects of temperature or frequency on the effective viscoelastic properties of UD composites (Pathan et al., 2017a,b; Liebig et al., 2019). Most research in the frequency domain examines composite behavior when the polymer is in the glassy state, often neglecting the temperature-dependent behavior from the viscoelastic glass transition to the rubbery state. In particular, there is a notable lack of studies linking fiber dispersion to the effective viscoelastic

properties of unidirectional composites at high temperatures, in the rubbery state. Furthermore, no studies have compared DMA experiments to predictions at high temperatures. Exploring the behavior of such composites at elevated temperatures is of interest for at least two reasons. First, since the time-temperature superposition principle applies to amorphous polymer matrices, long-term viscoelastic responses can be predicted by studying viscoelastic properties at high temperatures. Second, as the temperature increases, the phase contrast between the matrix and fibers becomes more pronounced, amplifying the effect of fiber arrangement.

In this study, we aim to characterize and predict the linear viscoelastic properties of unidirectional (UD) composites across a temperature range spanning from the glassy to rubbery states of the matrix. By considering this wide temperature range, we seek to better understand the relationship between microstructure and viscoelasticity at the macroscale, as it can be measured in the lab. Additionally, the attempt to use actual DMA experimental data to define the anisotropic behavior for structural calculations, such as finite element simulations, will reveal the challenges involved in this approach. The proposed two-step modeling procedure, which (i) estimates the homogenized behavior of the composite using full-field micromechanics modeling and (ii) reproduces DMA experimental tests through finite element simulations with the homogenized behavior as input, has not been attempted before. The homogenization step will extend the work of (Gusev and Kern, 2018) beyond the glassy state, enabling a more comprehensive investigation of the impact of fiber arrangement and a more complete comparison with mean-field model predictions, which have so far been limited to the glassy state. Additionally, it will address the presence of matrix-rich regions resulting from the fabrication process.

The manuscript is organized as follows. In the next section, the material is described, and experimental results are presented. Scanning electron microscopy (SEM) images were used to determine the fiber volume fraction, while DMA torsion tests characterized the structural shear moduli of the polymer matrix and the composite. In Section 3, a brief finite element analysis is conducted in linear elasticity to highlight the gap between the experimental measurements and the parameters required for the transversely isotropic stiffness matrix in mechanical calculations. Next, the two-step modeling procedure, which includes Fast Fourier Transform (FFT)-based homogenization and finite element simulations on homogeneous structures, is detailed. Section 4 presents the main results of the homogenization study. A

convergence analysis, in terms of number of fibers and fiber voxel resolution, is performed and may serve as a reference for future work. The impact of fiber spatial arrangement is also explored by comparing random and hexagonal distributions at different temperatures and fiber fractions. Finally, the last section presents the results of the finite element simulations of the torsion experiments, with comparisons to the experimental data. The influence of the microstructure, particularly fiber arrangement and the presence of matrix bags, is discussed.

2. Material microstructure and linear viscoelasticity characterization

2.1. Material

The material of interest is a UD composite produced by Arkema with T700S fibers all oriented in the same direction and embedded in thermoplastic Elium resin. The available information on the fibers includes their diameter, $7\mu m$, and a tensile modulus of 230 GPa in the fiber direction. As for the Elium matrix, in the glassy state, the Young modulus is 3 GPa, and the tensile strength is 54 MPa, while the glass transition temperature lies in the range of 115-120°C. The composite material was received as a 1.35 mm-thick plate. A plate of pure Elium resin was also prepared to characterize the linear viscoelasticity of the isotropic amorphous polymer matrix.

In order to characterize experimentally the matrix and composite viscoelasticities through dynamic torsion tests, slender rectangles of length $L = 55$ mm, width $W = 8$ mm and thickness t=1.35 mm were cut in both plates. Due to its unidirectional structure and the behaviors of the constitutive phases, the composite is transversely isotropic, hence the sample cutting direction matters. Defining θ, as the angle between the direction of the fibers and the direction of the sample length, specimens were cut at $\theta = 0°$, $45°$ and $90°$ and are referenced as UDθ (i.e. UD0, UD45 and UD90).

2.2. Composite microstructure analysis

After mechanical and ion polishing, followed by gold deposition, a transverse cross-section of the composite was observed using a field emission gun environmental scanning electron microscope (FEG-ESEM), model FEI Quanta 650. The resulting image, shown in Figure 1, reveals that the fibers are well-aligned, as indicated by their circular cross sections. Additionally,

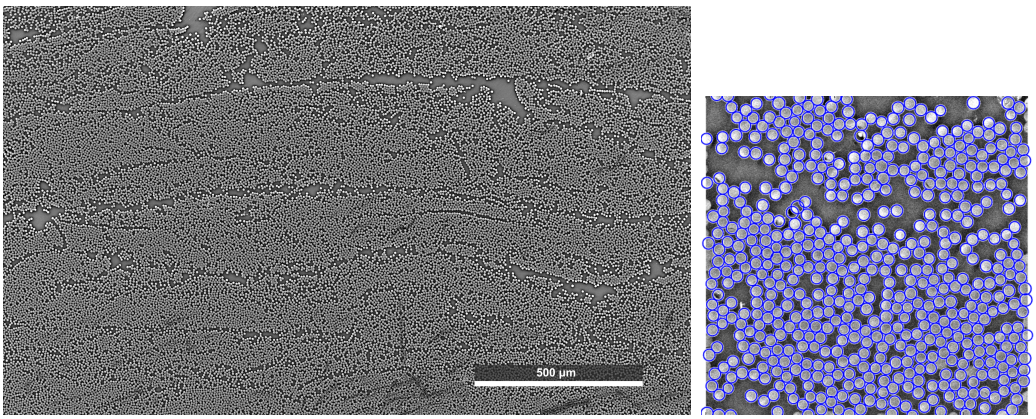

Figure 1: Scanning electron microscope image of a transverse cut of the composite and illustration of the automatic fiber detection.

the random distribution of fibers is not perfectly homogeneous, as regions of varying matrix sizes can be seen scattered throughout.

The grayscale contrast between the fibers and the matrix did not allow for direct image segmentation. Instead, a circle detection method was successfully employed to distinguish between the two phases (Figure 1). The fiber diameter was confirmed to be $7\mu m$ with no significant variation. By counting the number of detected circles, the fiber volume fraction was calculated. The chosen procedure involved selecting a random seed point in the image and defining a box in which the fiber volume fraction was measured. The box size was then gradually increased until convergence was reached for an area of 3 mm^2. Volume fraction estimates from four different seed points using the same approximate 3 mm^2 box size yielded a mean value of 53%, with a dispersion of approximately 2.5%.

2.3. DMA characterization of matrix and composites

Samples were submitted to DMA in torsion with a MCR502 rheometer from Anton Paar. Oscillations at $f = 1$ Hz and equilibrated temperatures were recorded for strain amplitudes ϵ_0 of 0.02% for the composite and 0.1% for the matrix. Three samples were tested for each material and orientation. Following the classical DMA analysis, an oscillatory rotation angle is applied as $\varphi(t) = \varphi_0 \sin(2\pi f t)$, resulting in a sinusoidal torque signal $\tau(t) = \tau_0 \sin(2\pi f t + \delta)$ where δ is the phase shift between the angle and the torque. It is convenient and common to work with complex quantities,

by defining $\tau^* = \tau_0.e^{i(2\pi ft+\delta)}$. Then, the torsion solution of Saint-Venant is applied,

$$G^* = G' + iG'' = \frac{3L\,\tau^*}{\varphi_0 W t^3(1 - 0.630(t/W))}, \tag{1}$$

with L, W and t the length, width and thickness of the sample, respectively. The storage shear modulus G' and the loss shear modulus G'' characterize the responses in-phase and out-of-phase with the applied strain. The shear storage and loss moduli are plotted with respect to the temperature in Figure 2 for the matrix and the composite samples. The error bars are small enough to be included in the symbol size.

The matrix and composite exhibit a viscoelastic transition between 90°C and 145°C. As expected, the composite is significantly stiffer than the matrix and its behavior is strongly influenced by the cutting angle relative to fiber alignment. Notably, the damping factor peaks occur at the same temperature for all samples, except for composite UD45. This suggests that the matrix's glass transition temperature remains unaffected when cured within the fibers. The slight shift towards a higher temperature observed in UD45 is likely due to some parameter coupling, which requires further investigation.

Another noteworthy feature is the intersections of the curves of UD0 and UD45 composite samples. At high temperatures, when the matrix is in the rubbery state, the storage and loss moduli of samples UD0, UD45 and UD90 are ordered from the higher to the lower values. At low temperatures, in the glassy state, UD0 shows values still above UD90 but below UD45. The latter result is in agreement with other data obtained on glassy UD composites submitted to quasi-static torsion experiments (Zhang and Hartwig, 1998; Adams and Bacon, 1973). Such an intersection between UD0 and UD45 has not yet been reported in the literature, and its explanation is not straightforward, particularly due to the sample being clamped at both ends, which significantly perturbs the strain field compared to simple torsion. Consequently, several material parameters contribute to the resulting stress.

In order to better understand the complexity of the experimental results at hand, we propose to reproduce the torsion test by finite element analysis, considering an elastic transversely isotropic material. This will show the difficulties to reach the composite behavior parameters and will prove the benefit of a micromechanics approach to predict the composite viscoelasticity.

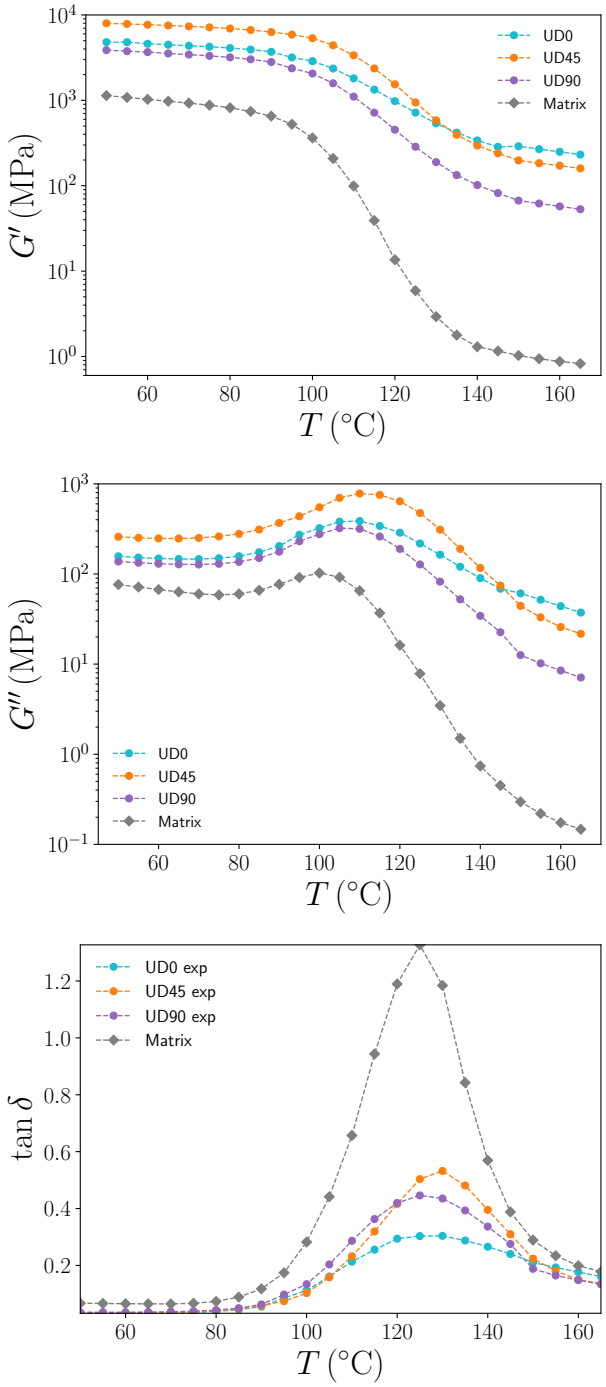

Figure 2: Storage modulus G', loss modulus G'' and damping factor tan δ, measured by 1 Hz torsion oscillation performed at equilibrated temperatures.

3. Motivation for the micromechanics approach

In this section, the response of a homogeneous transversely isotropic rectangular beam, submitted to torsion as in the rheometer, is explored by finite element analysis, in order to better understand the impact of the material behavior and the experimental boundary conditions on the resulting structural shear modulus. Then, a two-step modeling procedure, based first on FFT-homogenization to predict the transversely isotropic equivalent homogeneous behavior, and second on finite element modeling of the torsion test, is proposed to reproduce the experimental viscoelastic results.

3.1. Torsional response vs material transversely isotropic behavior and test boundary conditions

The composite, made of an isotropic matrix and isotropic or more likely transversely isotropic fibers all oriented in the same direction, is transversely isotropic and therefore five independent parameters characterize its mechanical behavior. Working in the frequency domain, the composite behavior may be described by a complex (*) compliance tensor $\underline{\underline{S}}^*$,

$$\underline{\underline{S}}^* = \begin{pmatrix} \frac{1}{E_T^*} & -\frac{\nu_{TT}^*}{E_T^*} & -\frac{\nu_{TL}^*}{E_T^*} & 0 & 0 & 0 \\ -\frac{\nu_{TT}^*}{E_T^*} & \frac{1}{E_T^*} & -\frac{\nu_{TL}^*}{E_T^*} & 0 & 0 & 0 \\ -\frac{\nu_{TL}^*}{E_T^*} & -\frac{\nu_{TL}^*}{E_T^*} & \frac{1}{E_L^*} & 0 & 0 & 0 \\ 0 & 0 & 0 & \frac{1}{G_{TL}^*} & 0 & 0 \\ 0 & 0 & 0 & 0 & \frac{1}{G_{TL}^*} & 0 \\ 0 & 0 & 0 & 0 & 0 & \frac{1}{G_{TT}^*} \end{pmatrix} \tag{2}$$

with temperature and frequency dependent complex parameters denoted: E_L^* for the longitudinal Young modulus in the fibers direction, E_T^* for the transverse Young modulus in the directions perpendicular to the fibers, G_{TT}^* the transverse shear modulus in the transverse plane (i.e. plane perpendicular to the fibers), G_{TL}^* the longitudinal shear modulus, ν_{TL}^* the longitudinal Poisson's ratio, and ν_{TT}^* the transverse Poisson's ratio with the relation $-\frac{\nu_{TT}^*}{E_T^*} = \frac{1}{2G_{TT}^*} - \frac{1}{E_T^*}$.

In order to assess if some of these parameters can be directly inferred from the DMA experiments, the torsional response of a transversely isotropic homogeneous material has been evaluated by finite element analysis for several sets of parameters. Moreover, the sample orientation characterized by the

angle θ has been mimicked by rotating the behavior fourth-order tensor. For the sake of simplicity, the study has been restrained in this subsection to linear elasticity. For purpose of comparison, the shear modulus G_0 is calculated as performed by the rheometer, using Saint-Venant approximation,

$$G_0 = \frac{3L\,\tau}{\varphi W t^3(1 - 0.630(t/W))}, \tag{3}$$

with φ the applied rotation angle and τ the resulting torque. As a reminder, the sample dimensions are equal to $L = 55$ mm, $W = 8$ mm and t=1.35 mm.

Simulations were performed on (Abaqus/Standard, 2021). Two types of Dirichlet boundary conditions were considered. The first one corresponds to Saint-Venant torsion conditions. The second one represents the actual boundary conditions of the DMA test, where both bottom and top surfaces are clamped and the top face is submitted to the torsion angle φ. In order to evaluate the impact of the experimental boundary conditions, the resulting torsional modulus calculated as in Eq. (3) has been evaluated for a fictive material with parameters, $E_L = 100$ GPa, $E_T = 1$ GPa, $G_{TL} = 3.5$ GPa, $\nu_{LT} = 0.35$ and $\nu_{TT} = 0.4$, for several angles θ. A sample length of 200 mm was chosen for the first boundary conditions in order to satisfy Saint-Venant assumptions of long specimens, while a length of 45 mm was chosen otherwise to match the experiments, the dimensions of the rheometer thermal chamber limiting the specimen length. Figure 3 shows how G_0 varies with respect to θ for both types of boundary conditions. The values of G_0 are significantly larger for the clamped specimen, except for $\theta = 90°$, where the moduli are similar. Additionally, Saint-Venant's conditions provide direct access to G_{TL} at $\theta = 0°$, unlike the experimental conditions, where restricted displacement along the torsion axis introduces a coupling between G_{TL} and E_L. Reducing G_{TL} from 3.5 GPa down to 2.5 GPa, while keeping all other parameters constant, results in a structural modulus of 3.5 GPa for the clamped specimen oriented at 0°.

Considering the experimental clamped boundary conditions only, and varying the material parameters, Figure 4 shows how G_0 is impacted by varying E_L, E_T and G_{TL}. The blue reference curve corresponds to the previously discussed case with $G_{TL} = 2.5$ GPa (instead of 3.5 GPa). Doubling E_T results in the green curve, where G_0 increases, except at $\theta = 0°$. The red curve corresponds to the same parameters as the reference blue curve, except for a significant reduction in G_{TL}. Doubling E_L, while keeping the same parameters as the red curve, produces the black plot. It is interesting

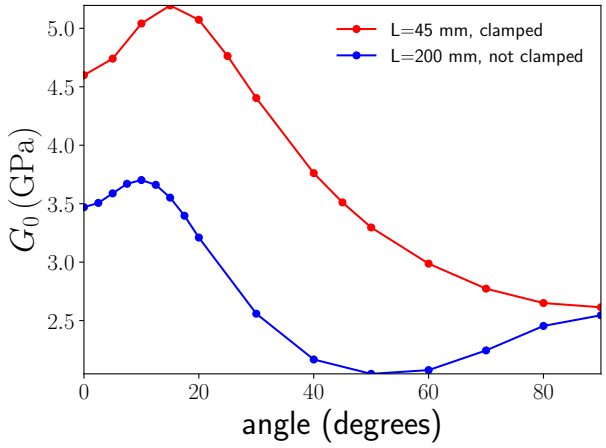

Figure 3: Impact of the test boundary conditions on the resulting torsional modulus G_0 (Eq. (3)) with respect to the angle θ between the sample length direction and the material longitudinal direction.

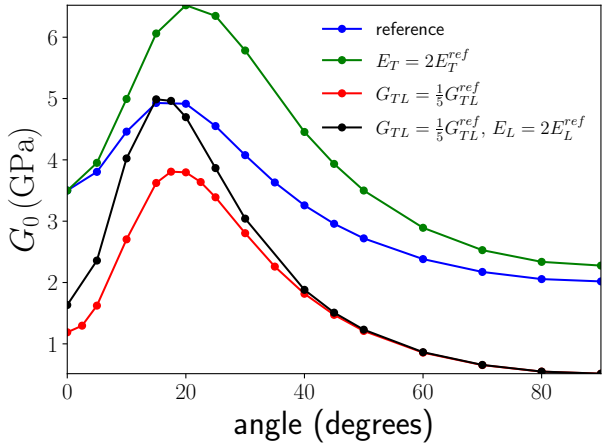

Figure 4: Impact of the transversely isotropic parameters on the shear modulus G_0 (Eq. (3)) with clamped boundary conditions as applied experimentally.

to note that the peak of G_0 occurs at a value of θ that depends on the material parameters. Moreover, the value of G_0 at $\theta = 0°$ is influenced not only by G_{TL} but also by E_L as discussed earlier, and appears independent of E_T. At $\theta = 90°$, G_0 is strongly dependent on G_{TL} and also on E_T as shown by the difference between the blue and green curves. Comparing the red and black curves shows that beyond $\theta = 40°$, the impact of E_L becomes negligible, while the impact of E_T is minimal below $\theta = 5°$. Finally, variations in the two other independent material parameters G_{TT} and ν_{TL}, induce less changes in G_0.

Figure 5 displays the evolution of G_0 at $\theta = 0°$ and $\theta = 90°$ with respect to G_{TL}, with all other material parameters remaining the same as in the reference case. This figure confirms that the shear modulus measured in torsion at both angles differs from G_{TL}.

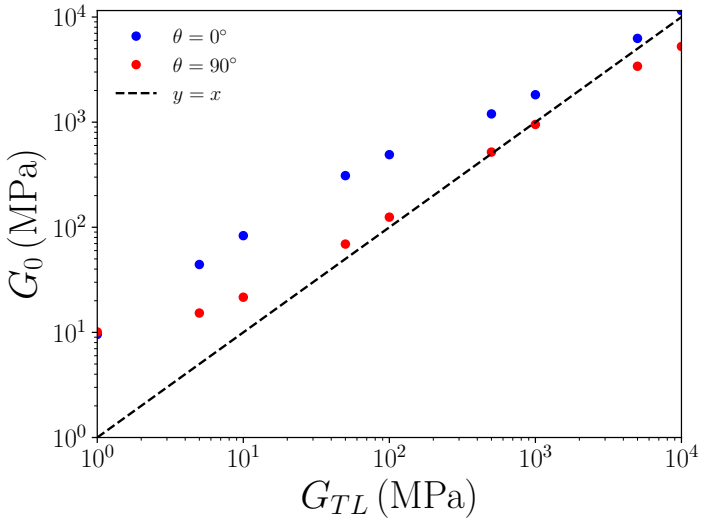

Figure 5: Finite element analysis of the torsional modulus at 0° and 90° with respect to G_{TL}. The values of the parameters are $E_L = 100$GPa, $E_T = 1$GPa, $\nu_{LT} = 0.35$ and $\nu_{TT} = 0.4$ (hence $G_{TT} = 0.357$GPa).

This numerical study highlights the fact that no parameter may be directly assessed from the experiments due to the strong coupling effects caused by restricted motion along the rotation axis imposed by the clamped grips. Moreover, the complex interactions between the parameters seem difficult to evaluate without a modelling approach. Therefore, we propose a two-step numerical modeling approach to determine whether the linear viscoelasticity

of the composite can be predicted based solely on the linear viscoelasticity of the matrix, the elasticity of the fibers and the fiber volume fraction.

3.2. Modeling procedure

The modeling procedure is illustrated in Figure 6. It consists in estimating

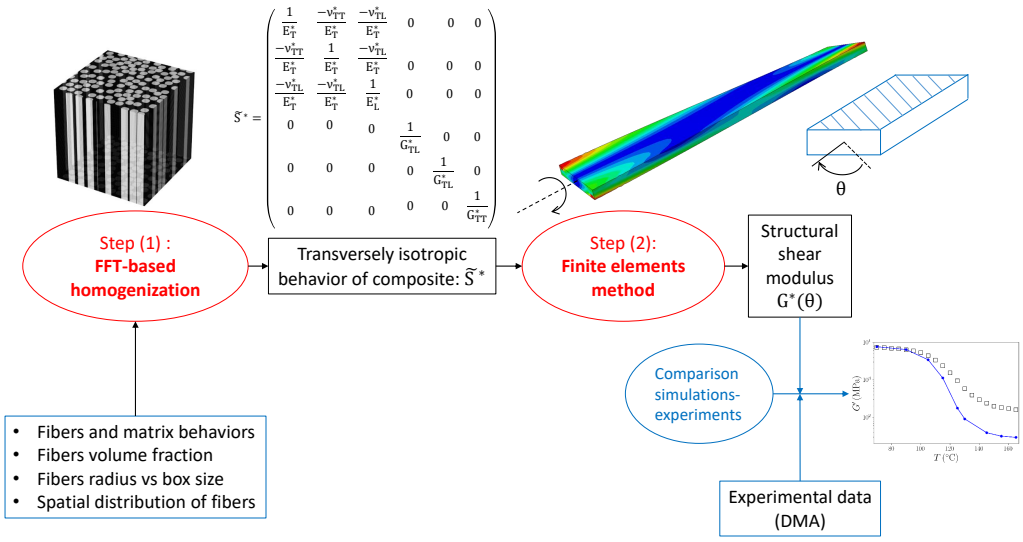

Figure 6: Modeling procedure to predict experimental data plotted in Figure 2. At each temperature, Step (1): FFT-based homogenization approach run in the frequency domain to assess the effective linear viscoelastic behavior of the composite. Step (2): Finite element simulation of the torsion test in the frequency domain with the effective behavior as input to estimate the structural modulus for UD0, UD45 and UD90.

the effective viscoelastic behavior of the composite by defining the compliance tensor in the frequency domain from simple FFT-based homogenization calculations run in complex. This step (1) is a full-field method which enables to replace the heterogeneous material by an equivalent homogeneous one, taking into account the mechanical behaviors and spatial arrangements of the phases. It has already been applied successfully for estimating the torsion modulus measured during temperature sweeps in heterogeneous polymers (Diani and Strauch-Hausser, 2021). Then, the predicted effective linear viscoelastic behavior of the composite, Eq. (2), is used as input in finite element simulations, Step (2), of the experimental torsion calculated in the

frequency domain, using the correspondence principle between linear elasticity and viscoelasticity in the harmonic regime (Hashin, 1970). This two-step procedure allows for the estimation of the structural shear modulus, G_0^*, for UD0, UD45 and UD90. When repeated for each temperature, from 50°C to 165°C with $\Delta T = 5$°C temperature steps, the theoretical results provide for a full comparison with the experimental data shown in Figure 2.

4. Frequency domain composite effective properties estimated by homogenization

The random microstructure generation and the numerical aspects of the Fast Fourier Transform (FFT)-based homogenization method are first described. Then, the mean-field model from (Hashin and Rosen, 1964; Christensen and Lo, 1979), which is defined for infinite cylinders embedded in a matrix, is presented for comparison purposes. The effective properties of the composite, in terms of the temperature-dependent storage and loss moduli, are calculated for random and hexagonal fiber distributions. Comparisons between the full-field calculations and the mean-field model predictions are discussed, as well as the impact of the fiber spatial arrangement, fiber volume fraction and fiber mechanical behavior that can be either isotropic or transversely isotropic.

4.1. FFT-based homogenization procedure

A full-field homogenization approach has been chosen to accurately estimate the linear viscoelasticity of the composite. In the frequency domain, the linear viscoelastic problem mirrors the linear elastic problem, where strain, stress, and behavior become complex quantities (Hashin, 1970; Gusev and Kern, 2018). Considering periodic realistic representations of the composite, their responses to simple shear and uniaxial tensile loadings are estimated thanks to the FFT-based homogenization method (Moulinec and Suquet, 1994, 1998) in order to reach the five parameters required to define $\underline{\underline{S}}^*$, as in Eq. (2), for the composite. The method is faster than the finite element approach for linear behavior and does not require meshing. Despite its advantages, only few studies have applied the FFT method to fiber composites (e.g. Wang et al. (2019); Sosa-Rey et al. (2023)). The model inputs are the mechanical behaviors of the constitutive phases and a 3D voxel grid representation of the periodic microstructure.

Focusing on harmonic loadings, the linear isotropic viscoelastic behavior of the matrix may be characterized by two parameters, G^* and K^*. The complex shear modulus, $G^* = G' + iG''$, has been determined by the dynamical torsion experiments at 1 Hz (section 2.3). Note that in order to account for the experimental gripped boundary conditions, the raw experimental outputs, as plotted in Figure 2, have been divided by a constant factor estimated at 1.1 following (Diani and Gilormini, 2017). The viscoelastic bulk modulus is significantly more difficult to measure and its dependence to temperature is limited compared to the shear modulus (Tschoegl et al., 2002). Therefore, it is commonly considered as purely elastic and independent on temperature. A typical value of $K = 3000\,\mathrm{MPa}$ was chosen. However, its limited impact has been tested and will be discussed later. Finally, the interface between the fibers and the matrix is modeled as perfect.

The carbon fibers are considered purely elastic and temperature independent. Since only the Young modulus is known to be 230 GPa, both isotropic and transversely isotropic carbon fibers are considered, using the values from another type of carbon fibers for the missing parameters (Soden et al., 1998). The elastic parameters are reported in table 1.

Transversely isotropic		Isotropic	
E_L (GPa)	<u>230</u>		
E_T (GPa)	15	E (GPa)	<u>230</u>
G_{TL} (GPa)	15		
G_{TT} (GPa)	7	ν	0.2
ν_{LT}	0.2		

Table 1: Elastic constants for the carbon fiber behavior. Input from the manufacturer is underlined, the other values comes from T300 carbon fibers (Soden et al., 1998).

The fiber arrangement may be extracted from SEM images (Figure 1). However, to extend the study to other fiber volume fractions, microstructures with randomly distributed carbon fibers were also generated numerically. For volume fractions below 55%, a random sequential addition (RSA) algorithm was used, while for volumes above 55%, a Monte Carlo Metropolis method was employed (Torquato, 2002). Figure 7 displays a random microstructure with a 53% fiber volume fraction generated by the RSA algorithm. Due to the microstructure's invariance in the fiber direction, the grid is restricted

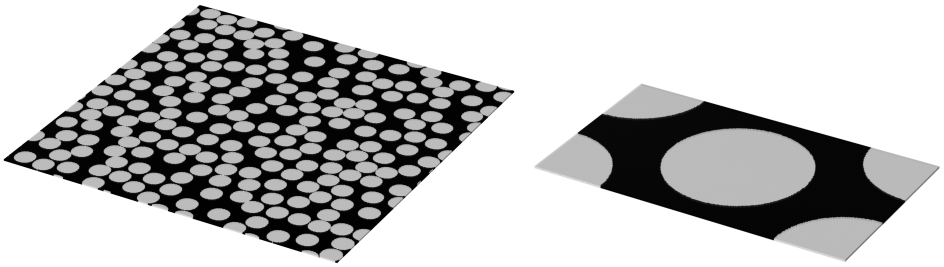

Figure 7: Random microstructure generated by a RSA algorithm (left) and hexagonal microstructure (right) for 53% volume fraction of fibers. The random microstructure contains 196 fibers of 30 pixels radius for a box size of 1024×1024×2 voxels. The hexagonal microstructure presents fiber of 76 pixels radius.

to a minimum of two pixels in that direction. Additionally, a hexagonal microstructure, where fibers are arranged periodically in a hexagonal array, was considered as an idealized transversely isotropic model (Li, 2001). The unit cell for this hexagonal arrangement with 53% fibers is also shown in Figure 7.

FFT-based calculations have consequently been run in complex using a python routine written by the authors and that could be shared upon request. For each temperature T, the Green operator is computed for an isotropic elastic reference material of parameters, $G_0 = \sqrt{G'_m(T)G_f}$ and $K_0 = \sqrt{K_m K_f}$ with $G_f = E_L/2(1+\nu_{LT})$ and $K_f = E_L/3(1-2\nu_{LT})$, for isotropic and transversely isotropic fibers calculations. A simple (Eyre and Milton, 1999) scheme has been applied to reach convergence. Simple shears according to the principal directions of the microstructure provide with estimates of G^*_{TT} once and G^*_{TL} twice. Simple uniaxial tensile loadings give two values of E^*_T and ν^*_{TL} and one value of E^*_L.

The accuracy of the full-field homogenization depends on the representativeness of the microstructure, which is characterized here by the number of fibers in the periodic box and the fiber resolution, or equivalently, the number of pixels per fiber radius. The latter parameter is akin to mesh fineness in finite element simulations. A convergence study was conducted with regard to both the number and resolution of fibers. In the most critical case, where fibers and matrix show the highest behavior contrast (at 165°C), the effective behaviors of 10 random microstructures with 53% fiber volume fraction were estimated. Figure 8 shows the values of the storage moduli E'_T and G'_{TL} as a function of the fiber radius in pixels. Each dot represents one

microstructure. A convergence plateau is observed at 30 pixels. Below this threshold, the moduli are overestimated. Increasing the number of fibers in the microstructure reduces the dispersion of the values, although the mean values of the effective moduli remain approximately the same.

Based on this convergence study, it was chosen that the 53% fiber random microstructures contain 196 fibers of 30 pixels radius for a box of 1024×1024×2 voxels. In what follows, considering the very low dispersion of the results for such a large number of fibers, each FFT-based result is based on one microstructure representation. For the hexagonal microstructure, 76 pixels per fiber radius were chosen without optimization since the microstructure is small enough and therefore simulations very fast. The final size of the box is $198 \times 344 \times 2$ voxels.

4.2. Mean-field models

Several mean-field models have been developped to predict the effective elastic properties of long fiber reinforced composites (Vignoli et al., 2019). These models, originally formulated for linear elasticity, can be extended to linear viscoelastic properties in the frequency domain, like the FFT-based homogenization approach. Recently, Gusev and co-authors (Hine and Gusev, 2019; Gusev and Kern, 2018) compared the 3-phase cylinder model, introduced by (Hashin and Rosen, 1964) and modified by (Christensen and Lo, 1979), with effective harmonic responses of unidirectional fiber-reinforced glassy composites obtained through finite elements. For transversely isotropic carbon fibers, the mean-field model accurately predicted the finite element results for both random and hexagonal microstructures, with a closer prediction for G^*_{TL} in the hexagonal representation. In the case of isotropic glass fibers, the mean-field model accurately reproduced the effective properties of the hexagonal array, and provided a reasonable estimate for the random microstructure, although there were underestimations up to 16% for C'_{ij} (real parts of $\underline{\underline{C}}^* = (\underline{\underline{S}}^*)^{-1}$). The finite element simulations also showed sensitivity to fiber arrangement when fibers were assumed isotropic, which diminished for transversely isotropic fibers.

While the former study puts a strong case for the 3-phase cylinder model, it was limited to glassy composites. The current study aims to extend this comparison to composites with a matrix in the rubbery state.

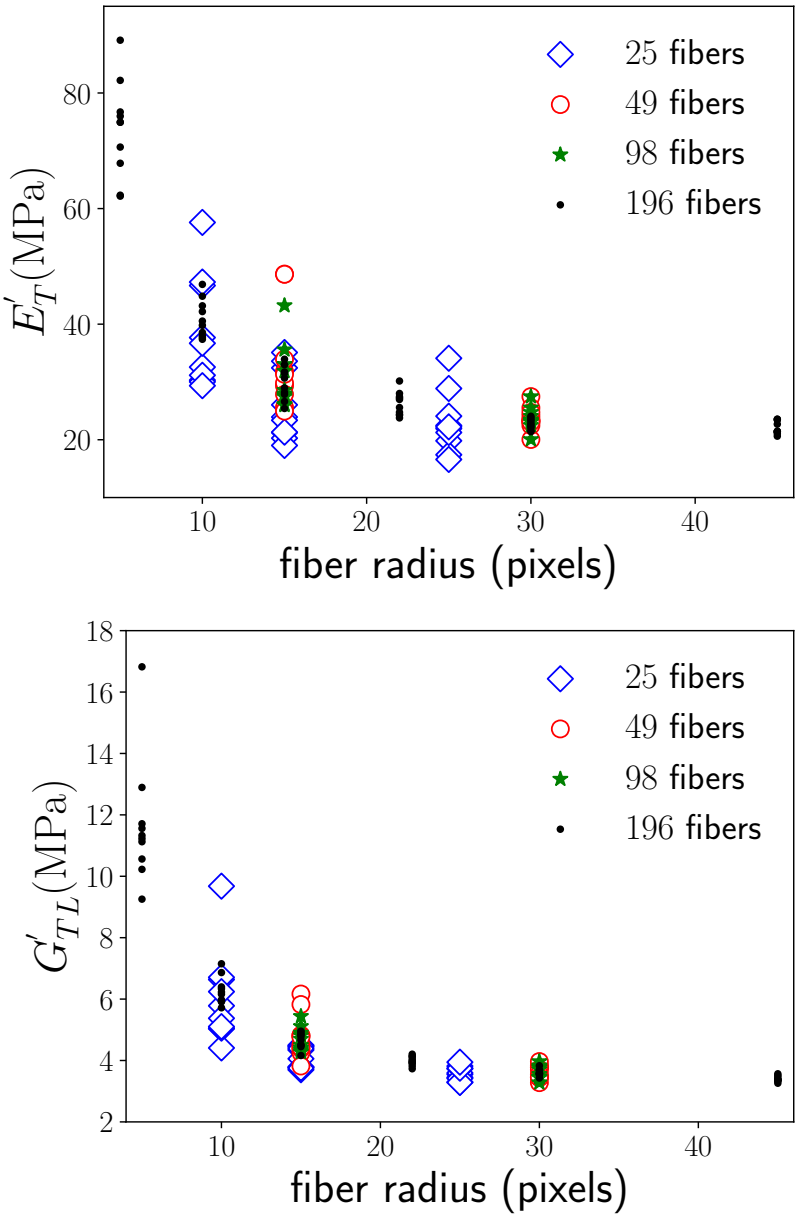

Figure 8: Convergence study in terms of the resolution of the fibers (number of pixel/radius) and number of fibers for the FFT-based numerical homogenization at $165°C$.

4.3. Results

The impact of the phase contrast is studied for 53% of fibers by calculating the storage and loss moduli characterizing the 1 Hz harmonic response of the composite for temperatures ranging from 50°C to 165°C, transitioning from the glassy to the rubbery states of the matrix.

4.3.1. Isotropic vs. transversely isotropic carbon fibers

Figure 9 shows the effective moduli E_T^*, G_{TL}^* and G_{TT}^* with respect to temperature obtained from the FFT-based homogenization method on random microstructures for isotropic and transversely isotropic carbon fibers. Note that the values of both the longitudinal modulus E_L^* and the longitudinal Poisson's ratio ν_{LT}^* are similar for every model and are close to the values predicted by a simple mixture rule (Voigt's bound). Therefore these parameters will not be represented nor discussed further (one can find $\nu_{TL}^* = \nu_{LT}^* \cdot \frac{E_T^*}{E_L^*}$ plotted in appendix B for transversely isotropic fibers as an illustration). Considering transversely isotropic carbon fibers instead of isotropic ones results in lower effective moduli, especially at low temperatures. This is a consequence of both the lower contrast between the fibers and the matrix at low temperatures, and the fact that transversely isotropic carbon fibers are less stiff than isotropic ones except in the longitudinal direction where both exhibit the same stiffness. Given that carbon fibers are more likely transversely isotropic (Soden et al., 1998), simulations are now performed with transversely isotropic fibers, unless explicitly specified.

4.3.2. Random vs. hexagonal microstructures

Figure 10 shows the effective moduli E_T^*, G_{TL}^* and G_{TT}^* with respect to the temperature for FFT calculations performed on random (full symbols) and hexagonal (open symbols) arrangements of fibers. The solid lines represents the mean-field estimates. The changes of E_T^* and G_{TT}^* for the hexagonal and random microstructures are similar at low temperatures but they differ significantly at temperatures higher than 115°C, the random microstructure exhibiting higher moduli than the hexagonal one. This difference increases with temperature, emphasizing the stronger impact of the fiber spatial distribution on the composite's effective properties at higher temperatures. For G_{TL}^*, the difference between both microstructures is less pronounced but follows the same trend with temperature. Despite being small, this difference is non-negligible at lower temperatures.

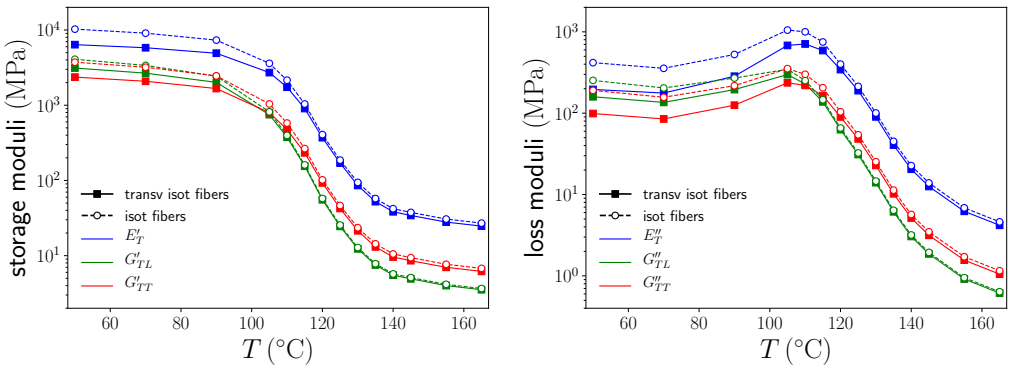

(a) (b)

Figure 9: Effective storage moduli (a) and loss moduli (b) with respect to temperature, estimated by FFT-based homogenization on random microstructures with isotropic fibers (dashed lines) and transversely isotropic fibers (continuous lines).

The mean-field 3-phase cylinder model accurately reproduces the random microstructure complex moduli E^*_T and G^*_{TT}, while it aligns well with G^*_{TL} for the hexagonal representation. This mismatched between the mean-field model and FFT results becomes more pronounced at higher temperatures.

In the case of isotropic carbon fibers, Gusev and Kern (2018) observed that the mean-field model's predictions were closer to those for the hexagonal array. We found the same result at low temperatures. At higher temperatures, however, while the mean-field prediction for G^*_{TL} remains accurate for the hexagonal microstructure, the predictions for E^*_T and G^*_{TT} fall between both microstructures, trending closer to the random representation (see appendix C, Figure C.18).

To better understand the impact of the microstructure arrangement, the local shear strain in the transverse plane (xy) has been plotted in Figure 11, in the case of microstructures submitted to an average transverse shear strain $\bar{\varepsilon}_{xy} \neq 0$ (every other $\bar{\varepsilon}_{ij}$ being nil) at 70°C and 125°C. For both random and hexagonal arrays, the fibers barely deform at 70°C and do not deform at all at 125°C. The strain field in the matrix is significantly more heterogeneous at 125°C than at 70°C, and it is also more heterogeneous in the random than in the hexagonal array. In particular, critically high local strain can be witnessed in the random microstructure at 125°C when two fibers nearly touch. At this high temperature, the ratio between the local and macroscopic strains can reach 55 in the random microstructure whereas it does not exceed

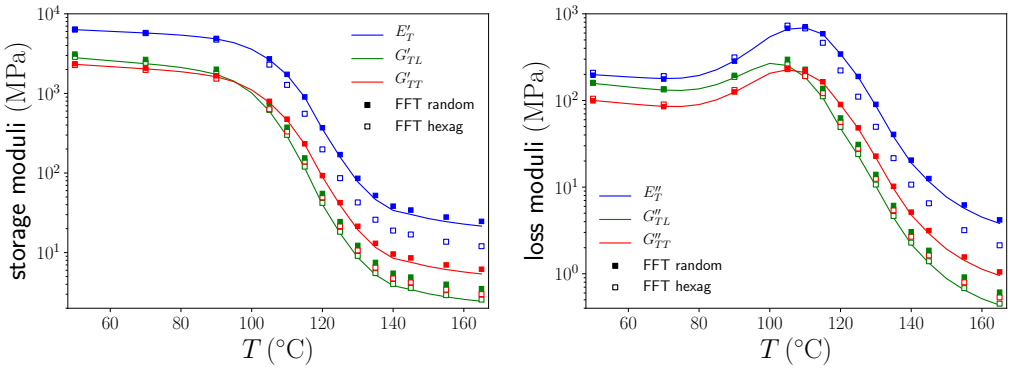

(a) (b)

Figure 10: Effective storage moduli (a) and loss moduli (b) with respect to temperature, estimated by FFT-based homogenization on random (full symbols) hexagonal (open symbols) arrangements and the mean-field prediction (solid lines) for transversely isotropic fibers.

8.6 in the hexagonal array. At 70°C this ratio does not exceed 7 and 3.7 for random and hexagonal microstructures, respectively.

As temperature rises, the phase contrast between the fibers and the polymer matrix increases, and the matrix becomes increasingly incompressible, with the ratio between the bulk modulus and the shear modulus rising significantly. To determine which change has the greatest impact on local strain heterogeneity and, consequently, on effective properties, FFT calculations were performed using a fictive matrix. This matrix had a temperature-dependent bulk modulus defined as $K_m(T) = K_m(T_0).\frac{G'(T)}{G'(T_0)}$ with $T_0 = 50$°C and $K_m(T_0) = 3000$ MPa, keeping its Poisson's ratio nearly constant. Results are presented in Figure 12. The random and the hexagonal arrays now yield nearly the same properties which are relatively well reproduced by the mean-field model at all temperatures, except for G^*_{TL}. Thus, the significant impact of the spatial distribution of fibers on the transverse moduli E^*_T and G^*_{TT} observed at high temperatures is primarily due to the matrix's quasi-incompressibility in the rubbery state. The smaller difference observed in G^*_{TL} remains unchanged and can be attributed to the phase contrast between the matrix and the fibers.

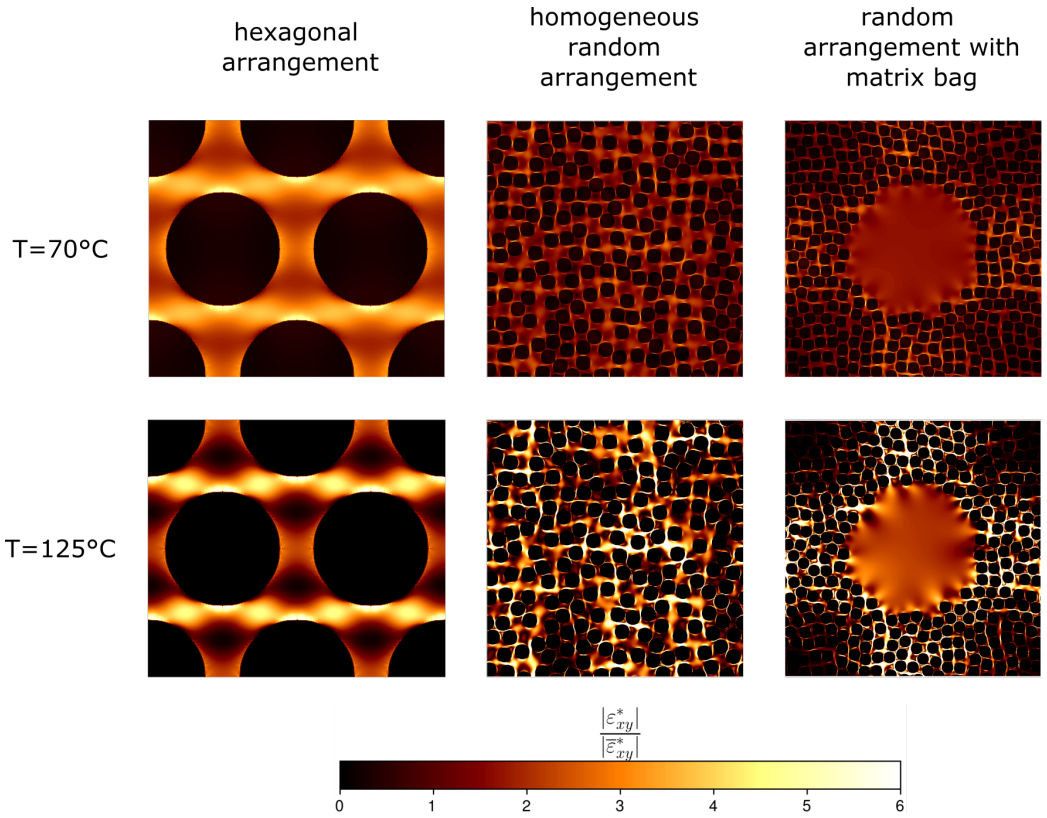

Figure 11: Normalized strain field $\frac{\varepsilon_{xy}}{\overline{\varepsilon}_{xy}}$ extracted from FFT calculations for hexagonal (left), random (middle) and random with circular matrix bags (right) microstructures. The considered temperatures are 70°C (top) and 125°C (bottom) and the fiber volume fraction is 53% in all cases.

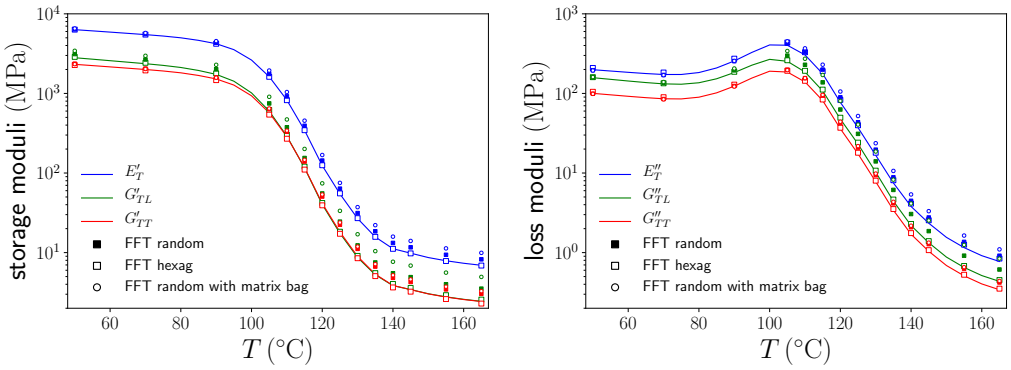

Figure 12: Effective storage and loss moduli of the composite with respect to temperature for a fictive matrix with its temperature-dependent bulk modulus varying such as its compressibility remains nearly constant.

4.3.3. Effect of fiber volume fraction

To go beyond the material of interest, the fiber volume fraction was varied from 10% to 80%. Figure 13 shows the composite effective moduli E^*_T, G^*_{TL} and G^*_{TT} with respect to the fiber volume fraction at 70°C and 125°C. The mean-field predictions (solid lines) are compared to the FFT calculations performed on random (full symbols) and hexagonal (open symbols) microstructures. The dispersion of results increases with both temperature and fiber volume fraction in the case of random microstructures. To address this, multiple FFT calculations (five in total) were performed and plotted for the two highest volume fractions considered (60 % and 69 %) at each temperature. This approach highlights the variability and helps validate the effectiveness of the mean-field predictions across different fiber distributions and temperatures.

At 70°C, when the matrix is in the glassy state, the effective moduli E^*_T and G^*_{TT} are relatively insensitive to the spatial arrangement of fibers across all volume fractions. Both are well-predicted by the mean-field model. The values of G^*_{TL} at 70°C also show independence from fiber distribution and are accurately captured by the mean-field model for volume fractions below 30%. For higher volume fractions, the mean-field model predicts the results of the hexagonal array and underestimates those of the random array, which is consistent with (Gusev and Kern, 2018). At 125°C and 165°C, when the matrix becomes nearly incompressible, significant differences emerge between the random and hexagonal microstructures starting at 30% fiber volume frac-

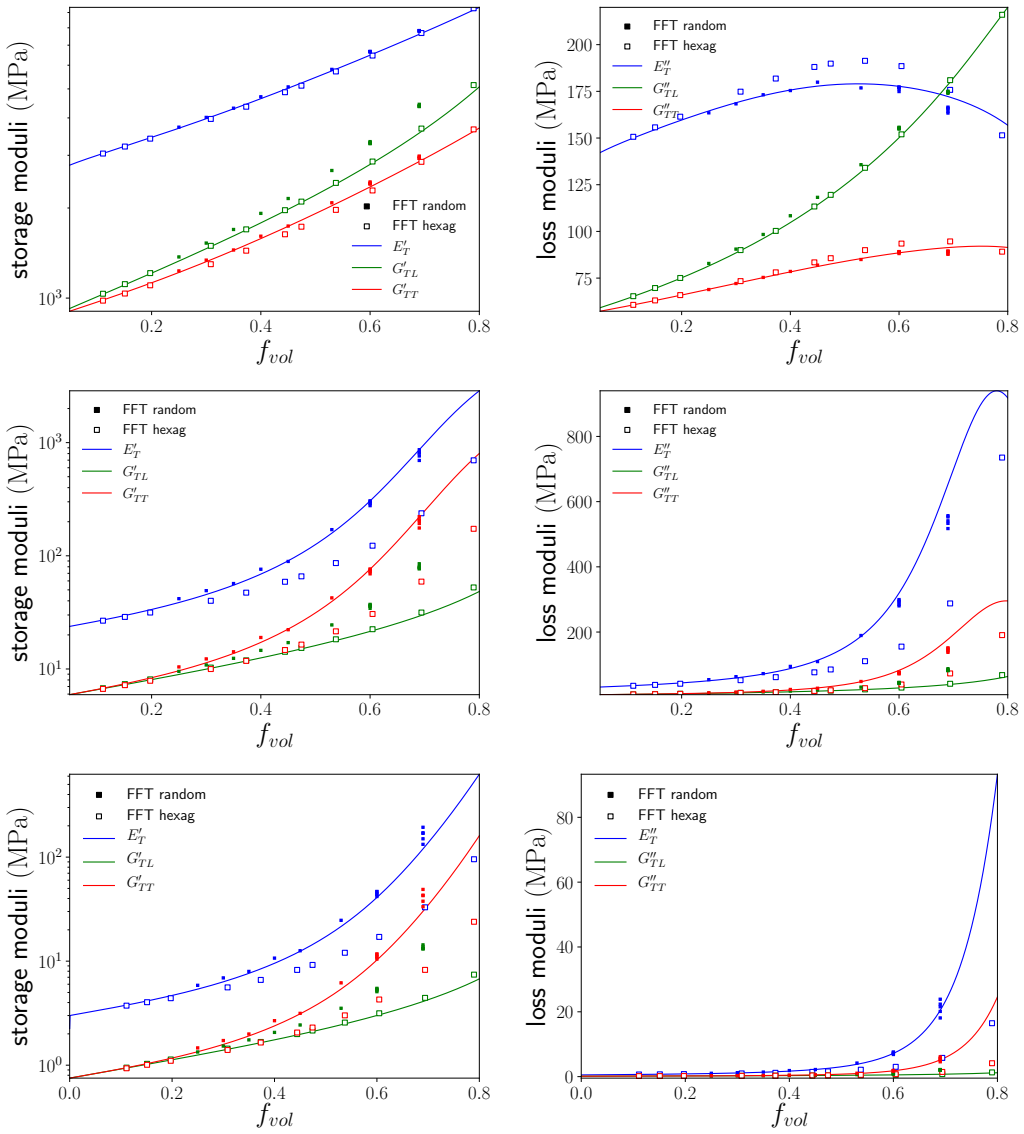

Figure 13: Effective storage and loss moduli of the composite as a function of fibers fraction, calculated at 70°C (top), 125°C (middle) or 165°C (botttom) for random (full symbols) and hexagonal (open symbols) microstructures and compared to the mean-field predictions (solid lines). Carbon fibers are considered as transversely isotropic.

tion. The mean-field model performs well in predicting E_T^* and G_{TT}^* for the random arrangement and G_{TL}^* for the hexagonal arrangement. However, it

becomes less accurate in predicting the loss moduli for high fiber volume fractions (above 60%) at 125°C.
In the case of isotropic carbon fibers, the mean-field model again predicts results closer to the hexagonal microstructure at low temperatures for all volume fractions, as previously observed by (Gusev and Kern, 2018). At higher temperatures, the model accurately reflects G^*_{TL} for the hexagonal packing and provides values for E^*_T and G^*_{TT} that lie between those for the two microstructures but are closer to the random packing across the fiber volume fractions considered (see appendix C, Figure C.19).

In exploring the effects of microstructure and constitutive phase behaviors on the transversely isotropic behavior of unidirectional composites in the frequency domain, we estimated the UD composite compliance tensor (Eq. (2)). It was calculated for the random microstructure with 53% of transversely isotropic fibers and is illustrated in Figure 9. Defined in the frequency domain at 1 Hz and varying with temperature, this tensor is the essential input for simulating and comparing experimental results from section 2.3 for UD0, UD45, and UD90.

5. Finite element simulations of UDθ torsion experiments

5.1. Simulation procedure

The corresponding principle between elasticity and viscoelasticity in the harmonic regime is used to simulate the DMA experiments. In the absence of volumetric forces and with Dirichlet boundary conditions only, the variational form of the problem reads as,
Find the complex displacement field $\underline{u}^*(x)$ *such that,*

$$\int_\Omega \underline{\underline{\sigma}}^*(\underline{u}^*(x)) : \underline{\underline{\varepsilon}}^*(\underline{v}^*(x))\, dx = 0,\ \forall \underline{v}^* \in \mathcal{U}_{ad} \tag{4}$$

where Ω refers to the material domain and $\mathcal{U}_{ad}$ to the field of admissible displacements. The linear viscoelastic behavior in the frequency domain is thus expressed as $\underline{\underline{\sigma}}^*(\underline{u}^*(x)) = (\underline{\underline{S}}^*)^{-1} : \underline{\underline{\varepsilon}}^*(\underline{u}^*(x))$ with $\underline{\underline{S}}^*$ the complex compliance tensor of the composite.

The torsion experiment was simulated with the partial differential equation solver FreeFem++ (Hecht, 2012), where the above variational form was implemented explicitly. The geometrical dimensions and the boundary conditions are the same as presented in the experimental section. A torsion angle

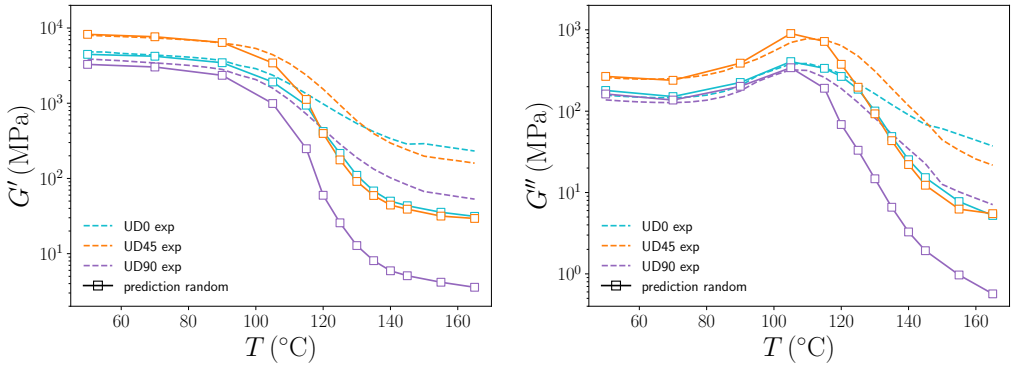

Figure 14: Comparison between the numerical (lines with symbol) and experimental (dashed lines) storage and loss moduli obtained by torsion tests on UD0, UD45 and U90.

is imposed in one of the clamped end, and the resulting complex torque is calculated to estimate the complex structural shear modulus with Eq. (1). To replicate the test with the different angles θ between the fibers and the sample (0°, 45° and 90°), the fourth-order compliance tensor is rotated to align the material basis.

After a quick convergence study, the mesh was set on $225 \times 40 \times 8$ ($L \times W \times t$) P2 triangular finite elements.

5.2. Results and discussion

Figure 14 compares the storage and loss moduli obtained by finite element simulations to the experimental measures for UD0, UD45 and UD90. At low temperatures, the numerical and experimental results coincide. Moreover, the intersection between UD0 and UD45 is reproduced, although at a lower temperature. However, at high temperatures, the numerical estimates appear well below the experimental data. One may note that the values of the structural shear modulus at 90° are similar to those of G^*_{TL}, which is likely coincidental as revealed by section 3.1.

At high temperatures, we showed that the fiber arrangement has a strong impact on effective properties. Therefore, a possible reason for the significant discrepancy between the model and the experiments stands in the fact that the actual material shows matrix bags (Figure 1) that have not been replicated in the random microstructure representation. The consequence of the presence of these bags is the existence of areas where the fibers are very close or touch each other, which is a source of large hydrostatic strain. In

zones without matrix bags, the volume fraction of fibers is obviously higher than 53%. One may read in Figure A.16 where a cut of the SEM image has been analyzed by the 2-point correlation function (Torquato, 2002), that the volume fraction of fibers reaches a much higher value of 67% in fiber dense areas. Therefore, in order to study the influence of the presence of matrix bags, a 53%-fiber microstructure with a large matrix area has been created by removing fibers at the center of a random microstructure with initially 67% of fibers (Figure 11). Considering a circular matrix bag at the center of the microstructure, does not provide perfect transverse isotropy since the bags form a cubic arrangement due to the periodic boundary conditions. However, according to our simulations, this simple strategy was enough to reach nearly transverse isotropic microstructures and enables us to estimate the trend in effective properties when accounting for matrix bags.

The effective properties of such a microstructure have been calculated in terms of E_T^*, G_{TT}^* and G_{TL}^*, as well as the resulting torsion moduli for UD0, UD45 and UD90, and compared to those of the 53% and the 67% randomly filled microstructures. Results are shown in Figure 15. The effective viscoelastic properties are not affected at low temperatures, however at high temperatures, the constitutive moduli significantly increase compared to the microstructure without a matrix bag and with the same volume fraction of fibers. At 165°C, the apparent fiber content that would lead to the same reinforcement in a random microstructure is as high as 60%. Figure 11 (right) shows the normalized strain field, $\frac{\varepsilon_{xx}}{\bar{\varepsilon}_{xx}}$, for the microstructure with a matrix bag subjected to a macroscopic uniaxial strain $\bar{\varepsilon}_{xx}$, all other macroscopic strains being nil. It can be seen that the local strain in the matrix, though higher than the average strain, is not as important as one could expect. The reinforcement noticed for the microstructure with the matrix bag may be compared to the case of carbon-black filled rubbers showing occluded (or trapped) rubber resulting in a higher effective amount of fillers (Medalia, 1972).

In the case of the fictive matrix with constant compressibility for all temperatures, the effective viscoelastic properties of the specific microstructure are plotted in Figure 12 (circles). It is obvious that the reinforcement for E_T^* and G_{TT}^* is significantly reduced at high temperatures, while the increase in G_{TL}^* remains consistent with the values observed when using a constant matrix bulk modulus. These results support our interpretation that the impact of fiber arrangement on effective properties is primarily due to matrix

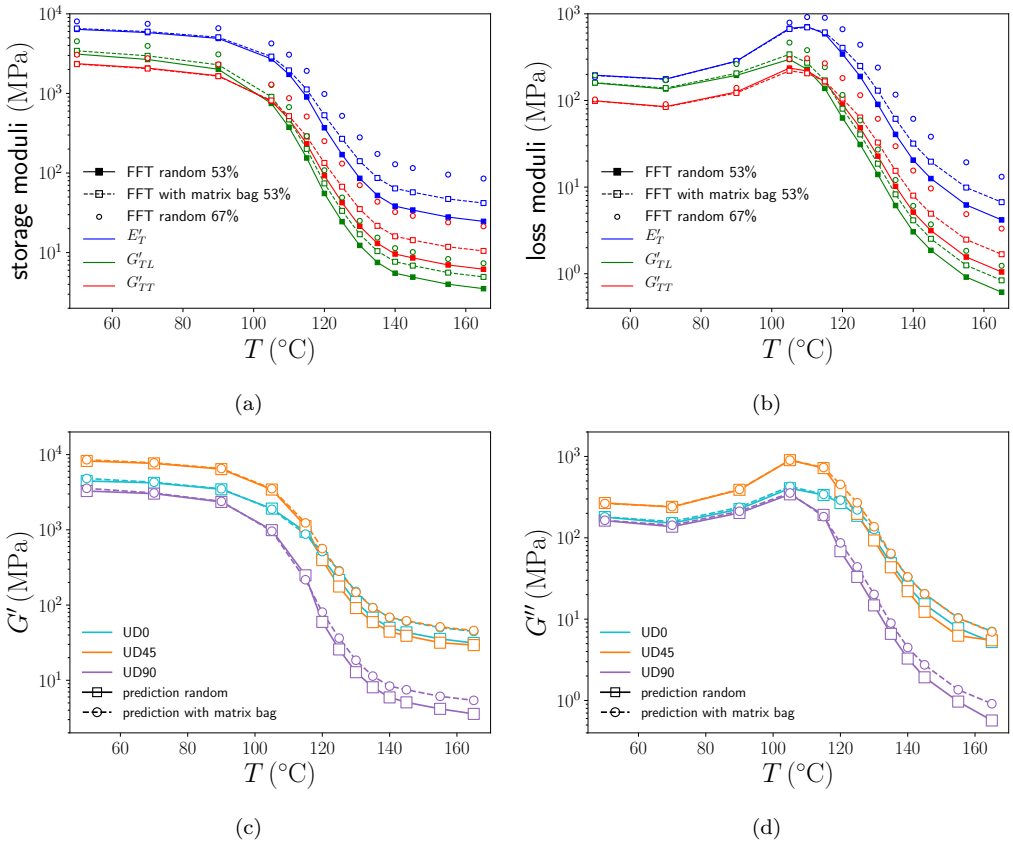

Figure 15: Impact of the presence of a matrix hole on FFT-based homogenization results (a and b) as well as on torsional moduli (e and f), with transversely isotropic carbon fibers. Storage and loss moduli are plotted on the left and on the right, respectively.

incompressibility for E^*_T and G^*_{TT}, and phase contrast for G^*_{TL}.

Finally, the torsion test was simulated for the effective viscoelastic parameters corresponding to the microstructure with a large matrix area at its center, as an input. In Figure 15, the results for the structural shear moduli for UD0, UD45 and UD90 are compared to the results plotted in Figure 14 for the random 53% microstructure. As expected, the storage and loss moduli remain unchanged at low temperatures but increase at high temperatures. While the trend is consistent with experimental observations, the magnitude of the increase is insufficient to fully reproduce the experimental results.

One might question whether incorporating an interphase region could provide sufficient reinforcement to bring the predictions closer to the ex-

perimental results. In this study, we did not account for the effect of an interphase with enhanced properties at the filler/matrix interface. Previous studies, such as (Feng et al., 2024), have reported an interphase thickness of approximately 200 nm in carbon fiber/epoxy composites, showing a gradient in mechanical properties from the fiber to the matrix. It is important to note that current experimental measurements of interphase thickness and mechanical properties using atomic force microscopy primarily offer qualitative insights. To roughly estimate the maximum potential impact of such an interphase on our results, we consider a scenario with a 200 nm interphase behaving like carbon fibers. This is equivalent to increasing the carbon fiber volume fraction from 53% to 59%, similar to the effect induced by the matrix bag. However, this scenario represents an upper bound for the potential enhancement of effective properties due to the interphase. The impact of a real interphase would be considerably lower due to the gradient in properties across the interphase and the unlikelihood of the polymer behaving like carbon fibers.

Hence, although the model performs well in the glassy state, which is the primary operational condition for these composites, there is still room for improvement to better predict the behavior in the rubbery state. This study emphasized the importance of considering both the boundary conditions of the torsion test to understand the ordering of structural shear moduli values based on the cutting angle and temperature, and the need for an accurate description of the spatial arrangement of fibers to achieve accurate effective properties and quantitative comparisons of the different structural moduli in the rubbery state.

6. Conclusion and perspectives

It has been reviewed that characterizing the linear viscoelasticity of an anisotropic unidirectional composite, consisting of a polymer matrix reinforced with long carbon fibers, presents significant challenges. Three-point bending DMA tests are inadequate for assessing material properties when the matrix softens at high temperatures, and torsion DMA tests involve clamping that introduces unwanted couplings between moduli in the measured torque. To address these challenges and accurately capture the linear viscoelastic behavior of such transversely anisotropic materials, we proposed an original two-step numerical procedure. This approach integrates micromechanics modeling and finite element simulations of the DMA structural test for model

validation. In the first step, the effective viscoelastic properties of the composite were assessed using full-field FFT-based homogenization, considering various fiber spatial arrangements. In the second step, the experimental dynamic torsion tests were simulated using the finite element method in the frequency domain, employing the elastic-viscoelastic correspondence principle for harmonic loading. The effective viscoelastic properties obtained from the homogenization were used as input for these simulations, enabling a direct comparison between predicted structural shear moduli and experimental data. Applying this two-step modeling procedure, several original and noteworthy results have been obtained, which are summarized below.

Micromechanics modeling results: The effect of the fiber spatial distribution within the matrix was evaluated through three different arrangements, hexagonal, uniformly random, and uniformly random with the presence of matrix bags. Both hexagonal and uniformly random arrangements were considered across various fiber volume fractions and a broad temperature range, corresponding to different phase contrasts as the polymer matrix becomes softer and nearly incompressible at higher temperatures. While the effective longitudinal modulus E_L^* and Poisson's ratio ν_{LT}^* appear largely insensitive to the microstructure, the transverse moduli G_{TT}^* and E_T^*, as well as G_{TL}^*, are notably affected. FFT calculations revealed that fiber arrangement impacts these effective properties at high temperatures and high fiber volume fractions. In such cases, the random arrangement produces larger moduli compared to the hexagonal array due to localized strain peaks in the matrix when fibers are closely spaced. The reinforcement mechanisms vary: matrix incompressibility primarily drives the increases in transverse moduli G_{TT}^* and E_T^* (absent at low temperatures), while phase contrast governs the behavior of G_{TL}^*.

For composites with transversely isotropic fibers, the mean-field 3-phase cylinder model accurately predicts G_{TT}^* and E_T^* for the random microstructure across all temperatures and fiber volume fractions. It also predicts G_{TL}^* for the hexagonal array consistently over the entire range of temperatures and fractions. For isotropic fibers, the mean-field model matches the hexagonal arrangement fairly well but underperforms for the random arrangement at low temperatures, in the glassy state. As temperature increases, the model accurately reproduces G_{TL}^* for the hexagonal array while it falls between the hexagonal and random representations for transverse properties, remaining closer to the random array.

The impact of the presence of matrix bags observed by scanning electron microscopy, was explored by introducing a pure matrix region into a random microstructure of 67% fibers, resulting in an average fraction of fibers of 53%. It was found that at a given fiber volume fraction, the presence of the matrix bags, while having minimal effect in the glassy state, leads to higher properties in the rubbery state.

Comparison with the experiments: The torsion moduli, characterized by DMA for composite samples cut at three different angles relative to fiber alignment, 0°, 45° and 90°, were estimated through finite element simulations using the effective properties computed by FFT on random microstructures. The moduli are accurately reproduced at low temperatures when the matrix is in the glassy state. Additionally, the storage and loss moduli calculated for samples cut at 45° are higher in the glassy state and lower in the rubbery state than those of samples cut at 0°, aligning well with experimental results, which exhibited a crossover in the measured moduli. However, at higher temperatures, the model predictions tend to underestimate the experimental results.

To further investigate this discrepancy, the structural modulus of the homogenized composite with the presence of matrix bags was also estimated. Although the reinforcing effect observed during the homogenization step brought the predictions closer to the experimental results, it was not sufficient to fully replicate them. Therefore, while the composite behavior has been well predicted in the glassy state, which is arguably the more likely state of use for this kind of materials, this study leaves room for improvement for predicting the behavior of UD composites at high temperatures by, for instance, taking into account the non-linear behavior of the matrix when local strain increases drastically.

Lastly, for UD composite manufacturers, it is important to note that the linear viscoelastic properties of their materials can be reasonably and efficiently assessed using the analytical three-phase cylinder model. However, it should also be remembered that microstructural heterogeneities will significantly influence the mechanical properties at high temperatures or equivalently during long-term responses.

Acknowledgement

The work has been supported by the Chair "Modelling advanced polymers for innovative material solutions" led by Ecole Polytechnique (l'X) and the Fondation de l'Ecole Polytechnique and sponsored by Arkema. Simulations were run on the Cholesky cluster from Ecole Polytechnique.

Appendix A. Covariances of generated and actual microstructures

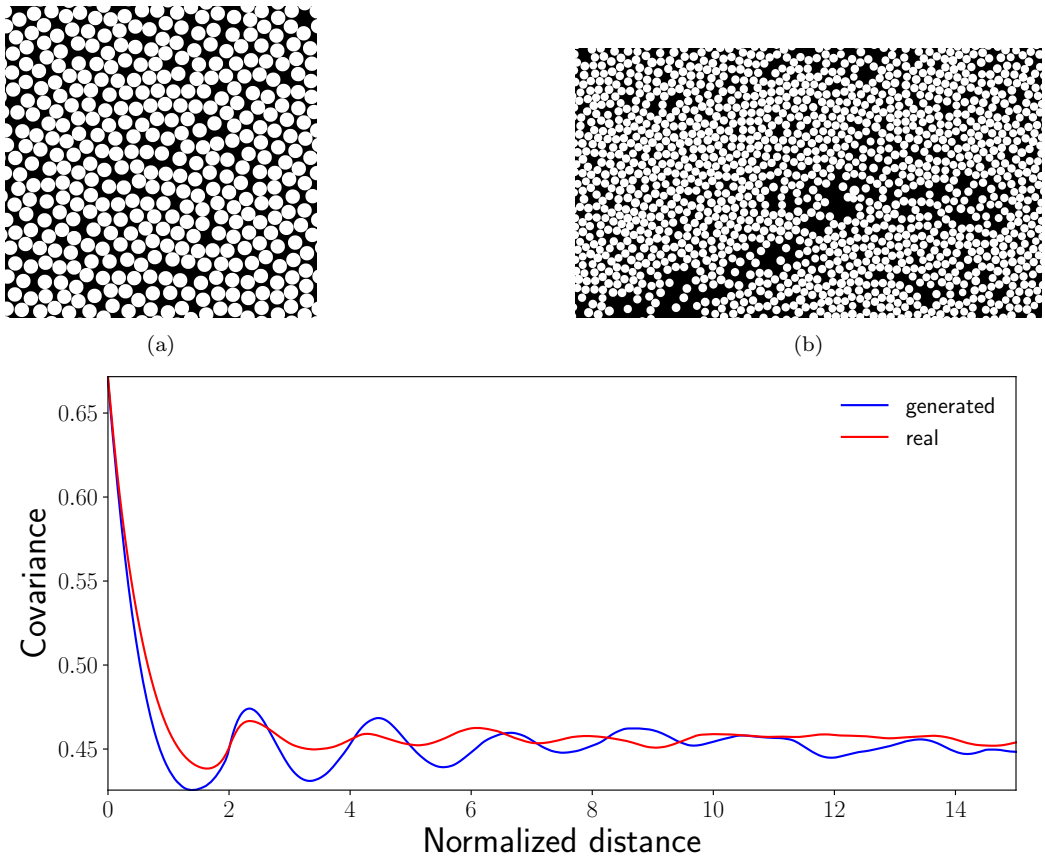

Figure A.16: Comparison between a real microstructure (b) and a microstructure generated by Monte Carlo Metropolis (a) and the corresponding covariances with respect to the distance normalized by the fiber radius (c).

Appendix B. Poisson's ratio as a function of temperature and volume fraction of fibers

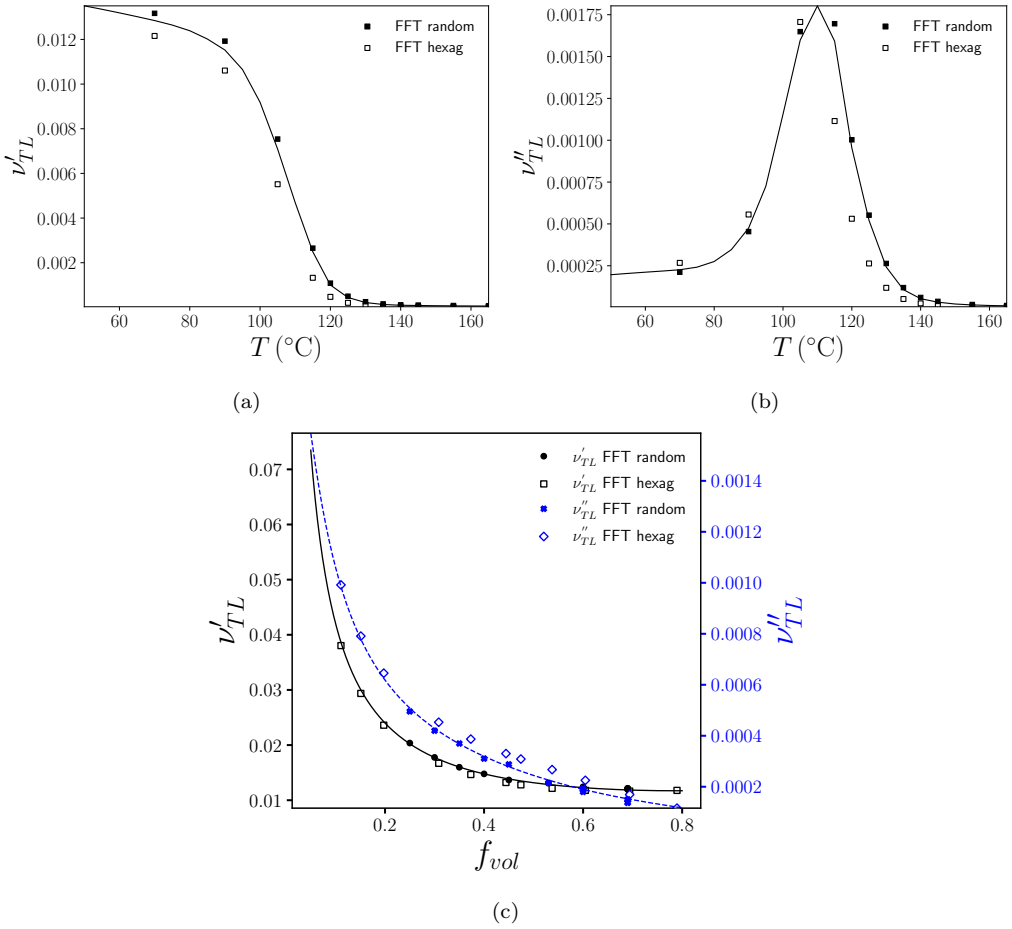

Figure B.17: Effective Poisson's ratio of the composite as a function of temperature at 53% fibers (a and b) or as a function of the fiber fraction at 70°C (c) for a random arrangement of transversely isotropic carbon fibers. Symbols correspond to results from FFT calculations whereas the curves represent the prediction by the 3 phase cylinder mean-field model.

Appendix C. Results of FFT-based homogenization simulations with isotropic fibers

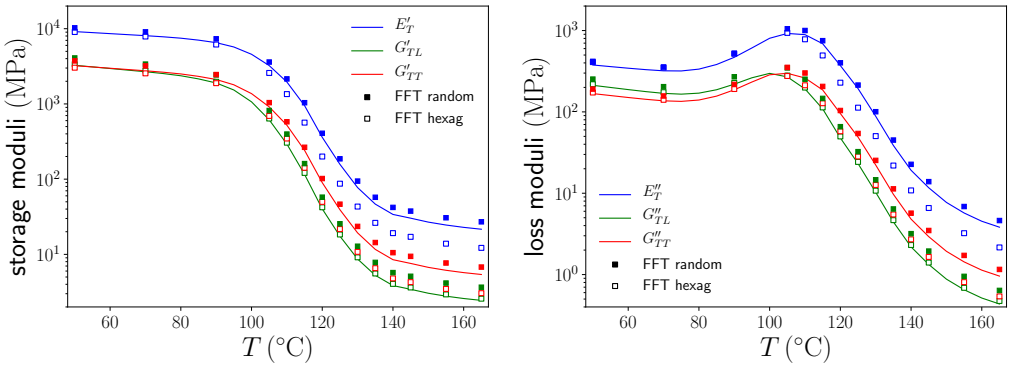

Figure C.18: Effective storage moduli (a) and loss moduli (b) with respect to temperature, estimated by FFT-based homogenization on random (full symbols) hexagonal (open symbols) arrangements and the mean-field prediction (solid lines) for isotropic fibers.

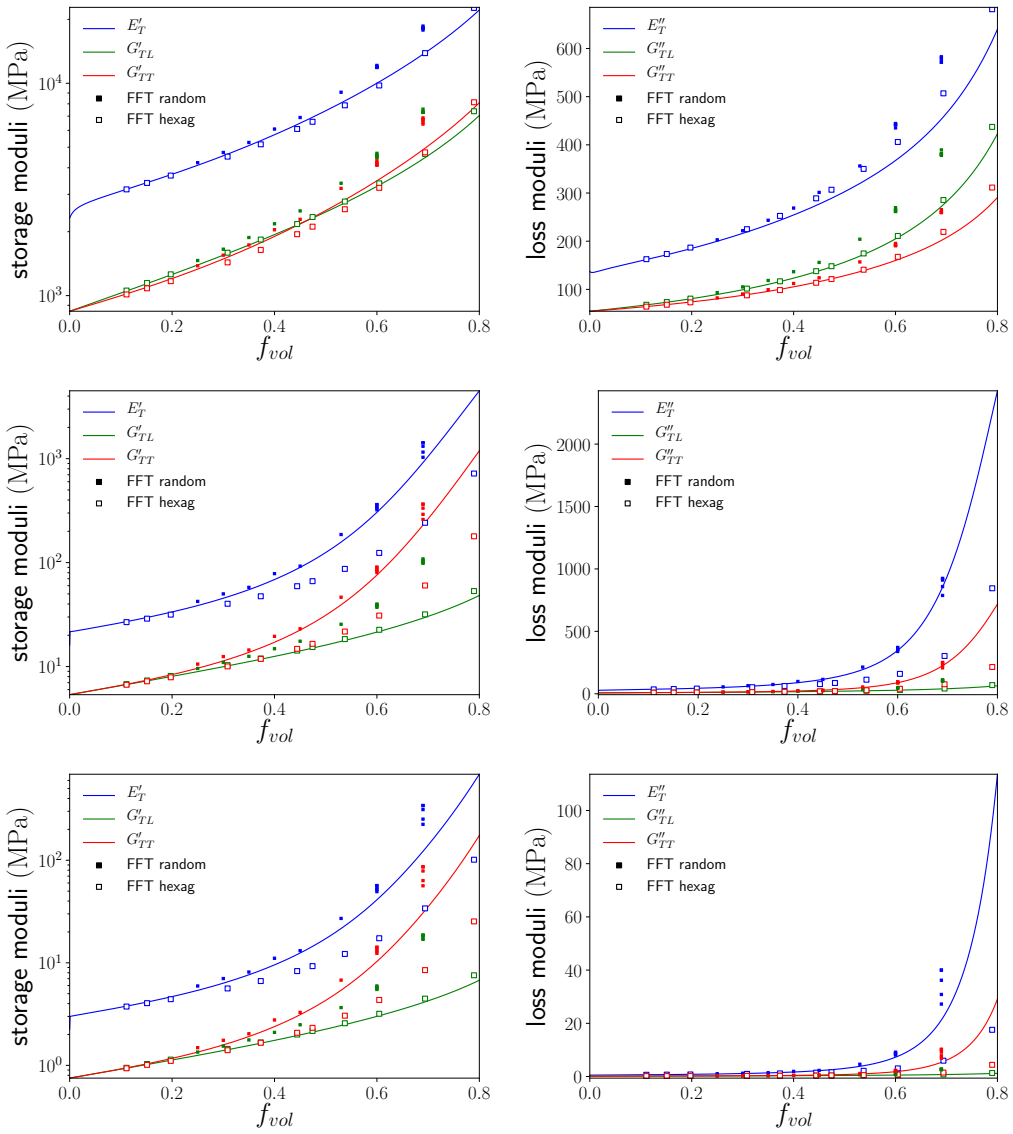

Figure C.19: Effective storage and loss moduli of the composite as a function of fibers fraction, calculated at 70°C (top), 125°C (middle) or 165°C (bottom) for random (full symbols) and hexagonal (open symbols) microstructures and compared to the mean-field predictions (solid lines) with isotropic carbon fibers.

References

Abaqus/Standard, 2021. Dassault Systèmes Simulia Corporation. Johnston, RI, USA.

Adams, R., Bacon, D., 1973. Effect of fibre orientation and laminate geometry on the dynamic properties of cfrp. Journal of Composite Materials 7, 402–428.

Beicha, D., Kanit, T., Brunet, Y., Imad, A., Moumen, A.E., Khelfaoui, Y., 2016. Effective transverse elastic properties of unidirectional fiber reinforced composites. Mechanics of Materials 102, 47–53.

Chamis, C.C., 1989. Mechanics of composite materials: past, present, and future. Composites Technology and Research 11, 3–14.

Christensen, R., Lo, K., 1979. Solutions for effective shear properties in three phase sphere and cylinder models. Journal of the Mechanics and Physics of Solids 27, 315–330.

Diani, J., Gilormini, P., 2017. On necessary precautions when measuring solid polymer linear viscoelasticity with dynamic analysis in torsion. Polymer Testing 63, 275–280.

Diani, J., Strauch-Hausser, E., 2021. Linear viscoelasticity of an acrylate ipn, analysis and micromechanics modeling. Soft Matter 17, 7341–7349.

Eyre, D., Milton, G., 1999. A fast numerical scheme for computing the response of composites using grid refinement. Eur. Phys. J. 6, 41–47.

Feng, P., Ma, L., Zhou, X., Li, M., Zhang, Q., Zhang, M., Liu, X., Jian, X., Xu, J., 2024. Constructing a gradient modulus interface layer on the surface of carbon fibers to enhance the mechanical properties of carbon fiber/epoxy composites at different temperatures. Composites Part B: Engineering 271, 111190.

Gusev, A.A., Kern, L.S., 2018. Frequency domain finite element estimates of viscoelastic stiffness of unidirectional composites. Composite Structures 194, 445–453.

Halpin, J.C., Tsai, S., 1969. Effects of environmental factors on composite materials .

Hashin, Z., 1970. Complex moduli of viscoelastic composites—i. general theory and application to particulate composites. International Journal of Solids and Structures 6, 539–552.

Hashin, Z., Rosen, B.W., 1964. The Elastic Moduli of Fiber-Reinforced Materials. Journal of Applied Mechanics 31, 223–232.

Hecht, F., 2012. New development in freefem++. Journal of Numerical Mathematics 20, 251–266.

Hine, P., Gusev, A., 2019. Validating a micromechanical modelling scheme for predicting the five independent viscoelastic constants of unidirectional carbon fibre composites. International Journal of Engineering Science 144, 103133.

Huang, Y., Jin, K.K., Ha, S.K., 2008. Effects of fiber arrangement on mechanical behavior of unidirectional composites. Journal of Composite Materials 42, 1851–1871.

Huang, Z.M., 2000. A unified micromechanical model for the mechanical properties of two constituent composite materials part ii: Plastic behavior. Journal of Thermoplastic Composite Materials 13, 344–362.

Huayamares, S., Grund, D., Taha, I., 2020. Comparison between 3-point bending and torsion methods for determining the viscoelastic properties of fiber-reinforced epoxy. Polymer Testing 85, 106428.

Lakes, R.S., 2004. Viscoelastic measurement techniques. Review of Scientific Instruments 75, 797–810.

Li, S., 2001. General unit cells for micromechanical analyses of unidirectional composites. Composites Part A: Applied Science and Manufacturing 32, 815–826.

Liebig, W.V., Jackstadt, A., Sessner, V., Weidenmann, K.A., Kärger, L., 2019. Frequency domain modelling of transversely isotropic viscoelastic fibre-reinforced plastics. Composites Science and Technology 180, 101–110.

Medalia, A., 1972. Effective degree of immobilization of rubber occluded within carbon black aggregates. Rubber Chemistry and Technology 45, 1171– 1194.

Melo, J.D.D., Radford, D.W., 2005. Time and temperature dependence of the viscoelastic properties of cfrp by dynamic mechanical analysis. Composite Structures 70, 240–253.

Mori, T., Tanaka, K., 1973. Average stress in matrix and average elastic energy of materials with misfitting inclusions. Acta Metallurgica 21, 571–574.

Moulinec, H., Suquet, P., 1994. Fast numerical method for computing the linear and nonlinear properties of composites. C. R. Acad. Sci. II 318, 1417–1423.

Moulinec, H., Suquet, P., 1998. A numerical method for computing the overall response of nonlinear composites with complex microstructure. Comp. Meth. Appl. Mech. Eng. 157, 69–94.

Oh, J.H., Jin, K.K., Ha, S.K., 2006. Interfacial strain distribution of a unidirectional composite with randomly distributed fibers under transverse loading. Journal of Composite Materials 40, 759–778.

Pathan, M., Patsias, S., Rongong, J., Tagarielli, V., 2017a. Measurements and predictions of the viscoelastic properties of a composite lamina and their sensitivity to temperature and frequency. Composites Science and Technology 149, 207–219.

Pathan, M., Tagarielli, V., Patsias, S., 2017b. Numerical predictions of the anisotropic viscoelastic response of uni-directional fibre composites. Composites Part A: Applied Science and Manufacturing 93, 18–32.

Ropers, S., Sachs, U., Kardos, M., Osswald, T.A., 2017. A thermo-viscoelastic approach for the characterization and modeling of the bending behavior of thermoplastic composites – part ii. Composites Part A: Applied Science and Manufacturing 96, 67–76.

Soden, P., Hinton, M., Kaddour, A., 1998. Lamina properties, lay-up configurations and loading conditions for a range of fibre-reinforced composite laminates. Composites Science and Technology 58, 1011–1022.

Sosa-Rey, F., Vella, C., Lingua, A., Pierre, J., Piccirelli, N., Therriault, D., Lévesque, M., 2023. Multiscale fast fourier transform homogenization of additively manufactured fiber reinforced composites from component-wise description of morphology. Composites Science and Technology 243, 110261.

Sun, C., Vaidya, R., 1996. Prediction of composite properties from a representative volume element. Composites Science and Technology 56, 171–179.

Swaminathan, G., Shivakumar, K., 2009. A re-examination of dma testing of polymer matrix composites. Journal of Reinforced Plastics and Composites 28, 979–994.

Torquato, S., 2002. Random heterogeneous materials: microstructure and macroscopic properties. Springer Science.

Treviso, A., Van Genechten, B., Mundo, D., Tournour, M., 2015. Damping in composite materials: Properties and models. Composites Part B: Engineering 78, 144–152.

Tsai, J.L., Chi, Y.K., 2008. Effect of fiber array on damping behaviors of fiber composites. Composites Part B: Engineering 39, 1196–1204.

Tschoegl, N., Knauss, W., Emri, I., 2002. Poisson's ratio in linear viscoelasticity – a critical review. Mechanics of Time-Dependent Materials 6, 3–51.

Vignoli, L.L., Savi, M.A., Pacheco, P.M., Kalamkarov, A.L., 2019. Comparative analysis of micromechanical models for the elastic composite laminae. Composites Part B: Engineering 174, 106961.

Wang, B., Fang, G., Liu, S., Liang, J., 2019. Effect of heterogeneous interphase on the mechanical properties of unidirectional fiber composites studied by fft-based method. Composite Structures 220, 642–651.

Xia, Z., Zhang, Y., Ellyin, F., 2003. A unified periodical boundary conditions for representative volume elements of composites and applications. International Journal of Solids and Structures 40, 1907–1921.

Younes, R., Hallal, A., Fardoun, F., Chehade, F.H., 2012. Comparative review study on elastic properties modeling for unidirectional composite materials, in: Hu, N. (Ed.), Composites and Their Properties. IntechOpen, Rijeka. chapter 17. URL: `https://doi.org/10.5772/50362`.

Zhang, Z., Hartwig, G., 1998. Low-temperature viscoelastic behavior of unidirectional carbon composites. Cryogenics 38, 401–405.